

Sedimentation of inertia-less prolate spheroids in homogenous isotropic turbulence with application to non-motile phytoplankton

M. Niazi Ardekani^{1,†}, G. Sardina^{1,2}, L. Brandt¹, L. Karp-Boss³,
R. N. Bearon⁴ and E. A. Variano⁵

¹Linné Flow Centre and SeRC (Swedish e-Science Research Centre), KTH Mechanics, SE-100 44 Stockholm, Sweden

²Department of Mechanics and Maritime Sciences, Chalmers University of Technology, 412 96 Gothenburg, Sweden

³School of Marine Sciences, University of Maine, Orono, ME 04469, USA

⁴Department of Mathematical Sciences, University of Liverpool, Liverpool L69 7ZL, UK

⁵Department of Civil and Environmental Engineering, University of California, Berkeley, CA 94720, USA

(Received 14 September 2016; revised 4 August 2017; accepted 15 September 2017;
first published online 13 October 2017)

Phytoplankton are the foundation of aquatic food webs. Through photosynthesis, phytoplankton draw down CO₂ at magnitudes equivalent to forests and other terrestrial plants and convert it to organic material that is then consumed by other planktonic organisms in higher trophic levels. Mechanisms that affect local concentrations and velocities are of primary significance to many encounter-based processes in the plankton, including prey–predator interactions, fertilization and aggregate formation. We report results from simulations of sinking phytoplankton, considered as elongated spheroids, in homogenous isotropic turbulence to answer the question of whether trajectories and velocities of sinking phytoplankton are altered by turbulence. We show in particular that settling spheroids with physical characteristics similar to those of diatoms weakly cluster and preferentially sample regions of downwelling flow, corresponding to an increase of the mean settling speed with respect to the mean settling speed in quiescent fluid. We explain how different parameters can affect the settling speed and what underlying mechanisms might be involved. Interestingly, we observe that the increase in the aspect ratio of the prolate spheroids can affect the clustering and the average settling speed of particles by two mechanisms: first is the effect of aspect ratio on the rotation rate of the particles, which saturates faster than the second mechanism of increasing drag anisotropy.

Key words: homogeneous turbulence, isotropic turbulence, particle/fluid flow

† Email address for correspondence: mehd@mech.kth.se

1. Introduction

The behaviour of suspended particles in turbulent flows is of considerable interest to a variety of processes, including dispersion of aerosols and collisions of water droplets in the atmosphere, dispersions of oil spills treated with dispersants, sediment transport and ecological processes in the plankton (see e.g. Guazzelli & Morris 2011). The latter is perhaps the least familiar to fluid dynamicists, but is of great importance because of the key roles plankton play in oceanic food webs, sustaining all the world's commercially important fisheries, and in global biogeochemical cycles, particularly the carbon cycle. Our interest here is in the behaviour of diatoms in turbulent flows. Diatoms are one of the largest and most significant groups of photosynthetic planktonic organisms in coastal and high-latitude environments. They are unicellular, but many species form colonies, often in the form of long chains and filaments, as shown in figure 1, making them an attractive model for studies on non-spherical particles in environmental turbulent flows. Diatoms are non-motile but they possess a siliceous cell wall that is denser than seawater (Eppley, Holmes & Strickland 1967), causing cells to be, generally, negatively buoyant. From an ecological perspective, sinking velocities and trajectories of diatoms in the upper mixed layer of the ocean are of a great interest, because of their effect on encounter-based processes in the plankton (e.g., prey–predator interactions, aggregate formation) and because the sedimentation of diatoms (as individuals or in aggregates) contributes to the shunting of CO₂ from the atmosphere into the deep ocean where it gets sequestered for thousands of years.

Sinking rates of diatoms have been largely measured in quiescent water (Smayda 1970), while in the surface layer of the ocean, where diatom reside, shear stresses applied by wind, breaking waves and thermal instabilities induce turbulence (Gerbi *et al.* 2009). Diatoms are typically smaller than or of the same size as the Kolmogorov length scale (Karp-Boss & Jumars 1998; Barton *et al.* 2014), hence our interest is in turbulence at the dissipation scale, which is supposedly independent of the production mechanism. Early observations that diatoms thrive in turbulence (Margalef 1978) and that stirring of cultures keeps cells in suspension lead to the notion that turbulence helps keep phytoplankton suspended and increases their residence time in the sun-lit surface layer of the ocean. Intriguing laboratory observations, however, suggest that turbulence enhances sinking velocities of at least some species of phytoplankton, including diatoms, relative to their still-water velocities (Ruiz, Macías & Peters 2004), but mechanisms remain illusive. Ruiz *et al.* (2004) proposed differential concentration as the mechanisms for the observed altered settling velocities, but this mechanism invoked results from systems with particles that are drastically different from diatoms (Wang & Maxey 1993; Wang & Stock 1993). Differential concentration in these studies is induced by particle inertia, leading to particle concentration in regions of downwardly moving fluid; however, diatoms and other phytoplankton are weakly inertial to follow the same physical mechanism.

Here we use a numerical model to examine whether rotation and orientation of diatoms in a turbulent flow can result in biased trajectories, enhanced sinking and preferential concentrations. While diatom morphologies are complex and may include spines and other projections (see figure 1), Nguyen *et al.* (2011) showed that in a simple shear flow the motion of a diatom with spines or projections could be well predicted from the theory of the motion of spheroids in a simple shear flow, providing that the cell is described by the smallest inscribing spheroid that encompasses both the cell and its spines. In a steady shear flow, a prolate spheroid spends most of its time aligned with the velocity vectors and tumbles with a predictable frequency

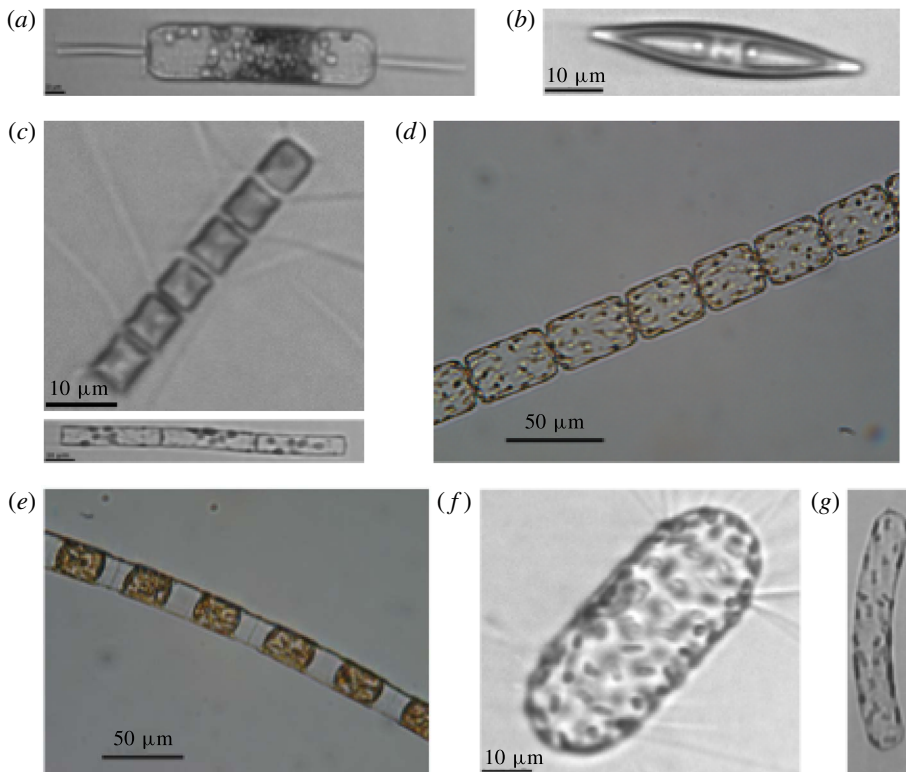


FIGURE 1. (Colour online) A mosaic of images of diatoms taken with a light microscope (*d* and *e*) or an Imaging Flow cytometer (*a*, *b*, *c*, *f* and *g*). (*a*) *Ditylum brightwellii* (*b*) *Navicula* sp. (*c*) *Chaetoceros* sp. (a chain-forming diatom), (*d*) *Lauderia annulata* (a chain-forming diatom), (*e*) *Lithodesmium undulatum* (a chain-forming diatom), (*f*) *Chorethron* sp., and (*g*) *Cylindrotheca* sp.

that is a function of its aspect ratio and the magnitude of the shear rate (Jeffery 1922). Observations on the motion of rigid diatom chains in a Couette flow show that they undergo periodic rotation, as predicted by theory (Jeffery 1922), with a period that increases with increasing chain aspect ratio (Karp-Boss & Jumars 1998). In unsteady shear and fully developed turbulent flows, the motion of axisymmetric particles becomes more complex, but a growing number of studies have advanced our understanding of the translation, rotation and orientation of dilute suspensions of small spheroids and fibres in turbulence, highlighting the rich dynamics of interactions (see the recent review by Voth & Soldati 2017). Important insights about the motion of neutrally buoyant rigid fibres in turbulence came from a study by Olson & Kerekes (1998). These authors used analytical approximations to derive translational and rotational dispersion coefficients for fibres in an isotropic stochastic flow field and showed a strong dependence of these coefficients on the fibre length. Using direct numerical simulations, Shin & Koch (2005) studied the translational and rotational motions of neutrally buoyant slender fibres in fully developed isotropic turbulence. Particles in their simulations ranged in size from tracer-like particles to fibres that are larger than the Kolmogorov scale. Their results show that fibres that are much smaller than the Kolmogorov length scale act as flow tracers and rotate like material lines.

With increasing length the fibre rotation rate attenuates as it becomes insensitive to the eddies that are smaller than the fibre length. The assuagement of the rotation rate was shown later to be associated with the tendency of rod-like particles to align more strongly with the vorticity vector than with the principal axis of strain (Pumir & Wilkinson 2011). Experimental measurements of rotation rates along the trajectories of short nylon threads in a turbulent flow are in agreement with model results (Parsa *et al.* 2012). Several studies have followed since, expanding the parameter space of this problem (e.g. Andersson, Zhao & Barri 2012; Parsa & Voth 2014; Byron *et al.* 2015; Ni *et al.* 2015). A common observation of these studies is the strong preferential alignment of anisotropic particles, either with the direction of the mean flow near a wall in turbulent channel flows (Zhang *et al.* 2001; Marchioli, Fantoni & Soldati 2010) or with the local velocity gradient tensor in isotropic turbulence, subsequently affecting rotational and translational motions.

The studies described above considered neutrally buoyant particles. For particles denser than the carrying fluid the presence of gravity adds further complication to the dynamics. The case of slender fibres sedimenting in a quiescent fluid has been the subject of many studies, see the review by Guazzelli & Hinch (2011). Most of these studies investigate the dilute regime, numerically (Mackaplow & Shaqfeh 1998; Butler & Shaqfeh 2002; Gustavsson & Tornberg 2009), whereas both dilute and semi-dilute regimes have been examined experimentally (e.g. Herzhaft *et al.* 1996; Herzhaft & Guazzelli 1999). The results show that in the dilute regime, a suspension loses its homogeneity, forming packets that are separated by sparse regions. In this regime the mean sedimentation velocity increases compared to the maximum velocity of an isolated fibre. In the semi-dilute regime, however, hindrance effects reduce mean velocity and the effect is stronger for a suspension of fibres than for a suspension of spheres. In both regimes the fibres are observed to orient in the direction of gravity (Herzhaft & Guazzelli 1999). Fewer studies have examined the problem of anisotropic particles settling in an external flow (i.e. not induced by the motion of the particles). Earlier studies have considered a cellular flow field and showed enhanced sedimentation of spheroids compared to spheres, and that at large aspect ratios tumbling become chaotic (Mallier & Maxey 1991; Shin & Maxey 1997). Siewert *et al.* (2014) used direct numerical simulations to study settling velocities of heavy ellipsoids in decaying isotropic turbulence. They found a preferential orientation with respect to the direction of gravity for prolate and oblate ellipsoids and a higher sedimentation velocity than that calculated from the orientation probabilities. Their study demonstrated that non-spherical, inertial particles experience a preferential sweeping mechanism, as was previously demonstrated for spheres (Wang & Maxey 1993; Toschi & Bodenschatz 2009; Gustavsson, Vajedi & Mehlig 2014; Bec, Homann & Ray 2014). The effect of turbulence on the settling of spheroids was found to be dependent on the turbulence level and the aspect ratio of the spheroid (see Siewert *et al.* 2014). In that study, all parameters were chosen to match ice particles in turbulent clouds, where the inertia of the particles is high. Diatoms and other phytoplankton represent the other extreme, anisotropic particles that are weakly inertial. Here we expand modelling efforts to the parameter space at which phytoplankton operate (see the [Appendix](#)).

We model diatom chains as prolate spheroids, using analytical and direct numerical simulations to examine if mean settling velocities of inertia-less diatoms are altered by turbulence. We begin by introducing the flow solver and the one-way coupling model used in this study to describe the particle motion in homogenous isotropic turbulence § 2. Next, we examine whether turbulence affects sinking velocities and clustering of

weakly inertial prolate spheroids, and how this may vary as a function of different particle parameters (§ 3). Alteration of sinking velocities is explained further in this section, considering a simple shear flow. The main conclusions and final remarks are drawn in § 4.

2. Governing equations and numerical method

2.1. Fluid phase

The incompressible turbulent velocity field, \mathbf{u} , obeys the Navier–Stokes and continuity equations:

$$\frac{\partial \mathbf{u}}{\partial t} + \mathbf{u} \cdot \nabla \mathbf{u} = -\nabla p + \frac{1}{Re} \nabla^2 \mathbf{u} + \mathbf{f}, \quad (2.1)$$

$$\nabla \cdot \mathbf{u} = 0. \quad (2.2)$$

Here t denotes the time, p the pressure, Re the Reynolds number and \mathbf{f} the random forcing field necessary to maintain the turbulent velocity in a statistically steady state. The equations are discretized in a cubic domain with periodic conditions at the boundaries. We employ direct numerical simulation (DNS) to solve all the relevant flow scales without any artificial model at the smallest scales. Since we evolve the equations in a three-periodic domain, it is natural to do so in Fourier space with a pseudo-spectral method. In this numerical scheme the nonlinear terms are evaluated in physical space using the classic 2/3 rule to minimize aliasing error. Time integration is performed with a third-order, low-storage Runge–Kutta method where the diffusive terms are analytically calculated (note that in Fourier space the Laplacian operator is proportional to the square of the modulus of the wave vector k^2) while an Adam–Bashforth-like approximation is employed for the nonlinear terms (Rogallo 1981). The stochastic forcing is evaluated in Fourier space and acts isotropically on the first shell of wave vectors. The forcing amplitude is constant in time and the field is delta-correlated in time and uniformly distributed in phase and directions (Vincent & Meneguzzi 1994). We employed a resolution of 128^3 grid points with a Taylor Reynolds number $Re_\lambda = 100$ and 64^3 grid points with a Taylor Reynolds number $Re_\lambda = 60$. The turbulence is characterized by the Taylor Reynolds number $Re_\lambda \equiv u' \lambda / \nu$, where u' is the root-mean-square of velocity fluctuations, ν is the kinematic viscosity and λ is the Taylor microscale, $\lambda \equiv \sqrt{\epsilon / 15 \nu u'^2}$, with ϵ the kinetic energy dissipation rate. The resolution was chosen so that the velocity gradients are well resolved since they drive the the equation of motion of the particles. Particle statistics are computed from independent samples separated by 1.6 turbulent Kolmogorov time scales, $\tau_f \equiv \sqrt{\nu / \epsilon}$, corresponding to about 300 configurations per particle. The numerical code has been already employed to study gyrotactic micro-organisms in homogeneous turbulence (Zhan *et al.* 2014) and rain droplet evaporation in clouds (Sardina *et al.* 2015).

2.2. Solution of the particle motion

The prolate spheroids studied here are small compared to the Kolmogorov length scale of the turbulence and have densities close to that of the carrier fluid. The translational relaxation time, τ_p , for prolate spheroids, assuming an isotropic particle orientation distribution is given by

$$\tau_p = \frac{2\rho_p a^2}{9\mu_f} \frac{\mathcal{AR} \ln(\mathcal{AR} + \sqrt{\mathcal{AR}^2 - 1})}{\sqrt{\mathcal{AR}^2 - 1}}, \quad (2.3)$$

with a the semi-minor axis of the prolate spheroid and \mathcal{AR} the aspect ratio (the ratio of polar over equatorial radii of the spheroid) (Shapiro & Goldenberg 1993). The time scale for the particles studied here is around three to four orders of magnitude smaller than the relaxation time of the turbulence flow around the particles. Furthermore, rotational relaxation times, concerning spinning and tumbling motions, are reported in the literature to be typically shorter than the translational relaxation time (Zhao *et al.* 2015; Marchioli, Zhao & Andersson 2016). With these operating parameters a tracer model for the particle motion is a suitable assumption (Shin & Koch 2005; Voth & Soldati 2017) and we, therefore, assume that the cells behave like passive tracers with a correction given by their Stokes settling velocity.

The particle translational motion obeys

$$\frac{d\mathbf{x}}{dt} = \mathbf{u}|_x + \mathbf{v}_s(\mathbf{p}), \quad (2.4)$$

$$\mathbf{v}_s(\mathbf{p}) = v_s^{\min} \hat{\mathbf{e}}_g + (v_s^{\max} - v_s^{\min}) (\hat{\mathbf{e}}_g \cdot \mathbf{p}) \mathbf{p}, \quad (2.5)$$

with \mathbf{x} denoting spheroid position, $\mathbf{u}|_x$ the fluid velocity at spheroid position, \mathbf{p} the spheroid orientation vector, \mathbf{v}_s the Stokes settling velocity and $\hat{\mathbf{e}}_g$ a unit vector in the direction of gravity. Here v_s^{\min} and v_s^{\max} are the minimum and maximum settling speeds in quiescent flow, corresponding to the particles falling with their major axis perpendicular or parallel to the gravity direction. These velocities can be written as

$$v_s^{\max} = \frac{(\rho_p - \rho_f) g l^2}{\mu_f} \gamma_0(\mathcal{AR}); \quad v_s^{\min} = \frac{(\rho_p - \rho_f) g l^2}{\mu_f} \gamma_1(\mathcal{AR}), \quad (2.6a,b)$$

with g the gravitational acceleration, l the length of the spheroid's major axis, μ_f the dynamic viscosity of the fluid, ρ_p and ρ_f the densities of the particle and the fluid. Here γ_0 and γ_1 are functions of the aspect ratio \mathcal{AR} , whose full expression can be found in Dahlkild (2011) among others.

The spheroid rotation follows the inertialess Jeffery equation

$$\frac{d\mathbf{p}}{dt} = \frac{1}{2} \boldsymbol{\omega}|_x \times \mathbf{p} + \alpha [\mathbf{I} - \mathbf{p}\mathbf{p}] \cdot \mathbf{E}|_x \cdot \mathbf{p}, \quad (2.7)$$

with $\boldsymbol{\omega}|_x$ the flow vorticity at the particle's position, \mathbf{I} the second-order identity tensor, $\mathbf{E}|_x$ the symmetric part of the velocity deformation tensor and α a function of the spheroid aspect ratio \mathcal{AR} , defined as

$$\alpha = \frac{\mathcal{AR}^2 - 1}{\mathcal{AR}^2 + 1}. \quad (2.8)$$

To solve the equations above, the flow velocity, vorticity and velocity gradients at the particle positions are calculated with a second-order interpolation scheme and a high enough resolution to capture the flow velocity gradients. The same Runge–Kutta scheme used for the carrier phase is employed to perform the time integration of (2.4) and (2.7) with a small enough time step ($\approx 0.001\tau_f$) to capture the time evolution of particle orientations via a formulation based on quaternions. We evolve a total of 200 000 spheroids for each simulation.

\mathcal{AR}	1	2	3	5	10	15	20
v_s^{max}	3.03	3.17	3.11	2.90	2.46	2.18	1.97
v_s^{min}	3.03	2.77	2.53	2.18	1.71	1.46	1.29
v_s^{max}/v_s^{min}	1.00	1.14	1.23	1.33	1.44	1.49	1.53
v_s^{iso}	3.03	2.90	2.72	2.42	1.96	1.70	1.52

TABLE 1. Maximum, minimum and average of settling velocities in quiescent flow, scaled with the Kolmogorov velocity for the investigated cases versus different aspect ratios. Here $\rho_p/\rho_f = 1.05$ and $D_{eq} = \eta/6$.

3. Results

We first investigate the settling of prolate spheroidal particles of constant volume, focusing on the effect of the particle aspect ratio. The parameters used are $Re_\lambda = 100$, $\rho_p/\rho_f = 1.05$ and $D_{eq} = \eta/6$, where D_{eq} is the diameter of a sphere having the same volume as the prolate spheroid and η is the Kolmogorov length scale. Fixing the volume, the settling speed varies with the aspect ratio. It should be noted that for the higher-aspect-ratio cases examined here ($\mathcal{AR} \geq 15$), the larger diameter of the spheroid exceeds the Kolmogorov length scale η (≈ 1.24 for $\mathcal{AR} = 24$). This does not violate our assumption of a tracer particle since rods act as tracers when their length is less than 5η and deviations from the tracer behaviour are very small until about 15η (Parsa & Voth 2014). For the simulations presented here, the average settling speed of an uniformly distributed suspension, v_s^{iso} , varies in the range $1.5\text{--}3u_\eta$. Table 1 shows the settling velocities for the investigated cases. The reported values are all normalized by the Kolmogorov velocity. Note that the average settling speed v_s^{iso} for spheroids in a quiescent flow is calculated as

$$v_s^{iso} = \frac{(v_s^{max} + 2v_s^{min})}{3}, \quad (3.1)$$

based on the assumption that the orientation of spheroids (cosine of the angle between spheroid's symmetric axis and the gravity direction) is uniformly distributed.

The results of the simulations are shown in figure 2. The main observation is that within the parameter space relevant to diatom chains, settling spheroids weakly cluster (figure 2a) and preferentially sample regions of downwelling flow, leading to downward velocity biases of up to 10% of the Kolmogorov velocity u_η (figure 2b). This corresponds to an increase of the mean settling speed of about 5% compared with the mean settling speed in quiescent fluid (figure 2c). These effects increase with the aspect ratio, \mathcal{AR} , and saturate for $\mathcal{AR} \geq 10$. In studies regarding unstable settling suspensions (Koch & Shaqfeh 1989; Herzhaft *et al.* 1996; Mackaplow & Shaqfeh 1998; Herzhaft & Guazzelli 1999), the enhanced sedimentation velocity is explained by two mechanisms. First, the preferential concentration in downwelling flow (as also observed in this study) and, second, the preferred orientation parallel to the gravity direction that causes fibres to settle faster. In these studies, the velocity disturbances due to the settling particles produce vertical shearing motion, which causes the preferential orientation. In the present study, however, the turbulent flow remains isotropic due to the one-way coupling assumption and the second effect cannot be observed. Therefore, the increase in the settling speed can be only attributed to preferential sampling of regions with downwelling flow.

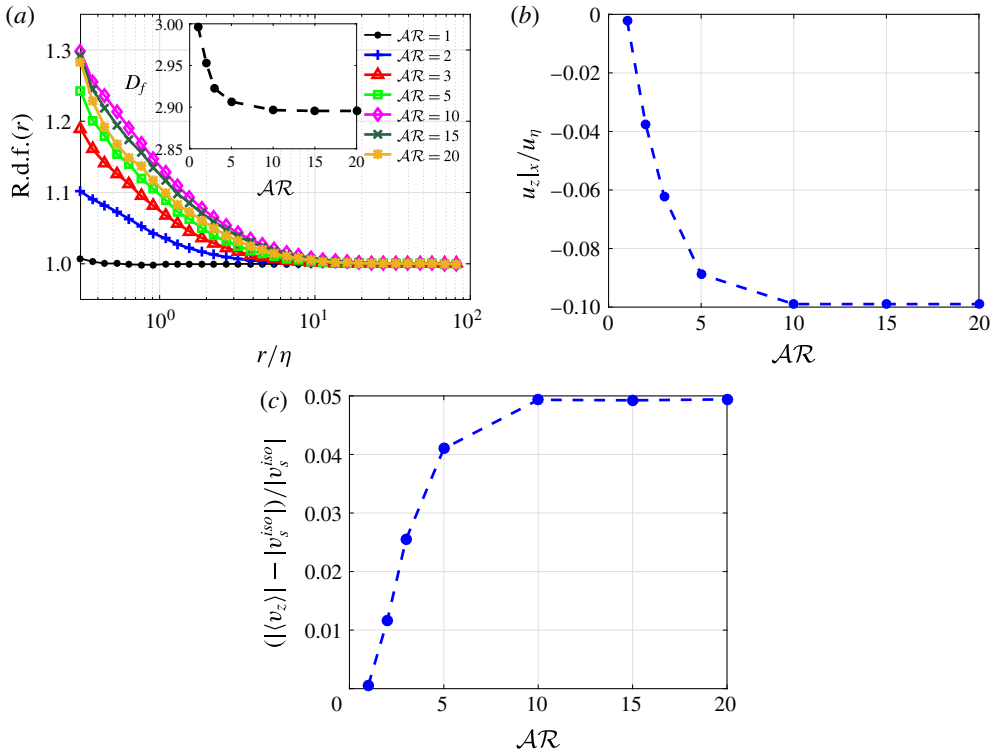


FIGURE 2. (Colour online) (a) Radial distribution function of particle positions; the inset in this panel reports the fractal dimension of the clustering, estimated by fitting the r.d.f. with a power-law in the range $r/\eta = [0.2:2]$, (b) average of fluid vertical velocity at the particle position and (c) increase in the settling velocity (difference in the settling rate with respect to the quiescent settling average v_s^{iso} , normalized by v_s^{iso}).

To quantify patchiness (clustering) in fully three-dimensional isotropic turbulent flows, we use the radial pair distribution function (r.d.f.), sometimes also called the correlation function. The r.d.f. measures the probability of finding a particle pair separated by a given radial distance, normalized by the value expected from a uniform distribution. This is defined as

$$g(r) = \frac{1}{4\pi r^2} \frac{dN_r}{dr} \frac{1}{n_0}, \quad (3.2)$$

where $n_0 = 0.5N_p(N_p - 1)/V_0$ is the density of pairs in the whole volume V_0 . N_p is the total number of particles in the domain and N_r is the number of pairs at distance r . The small volume fraction, used here, removes the exclusion effects, and thus an r.d.f. for a random distribution results in a flat value of 1. The r.d.f. is reported in figure 2(a). In the inset of the same figure, we report the scaling exponent of the r.d.f. at small separations, also often used as an indicator of patchiness (Durham *et al.* 2013). This exponent denotes the fractal dimension of the set where particles are found. Patchiness is seen to increase with the particle aspect ratio and saturate at the largest values considered. However, a fractal dimension 2.9 shows weak clustering. Increasing the aspect ratio, while keeping the volume and the density ratio constant,

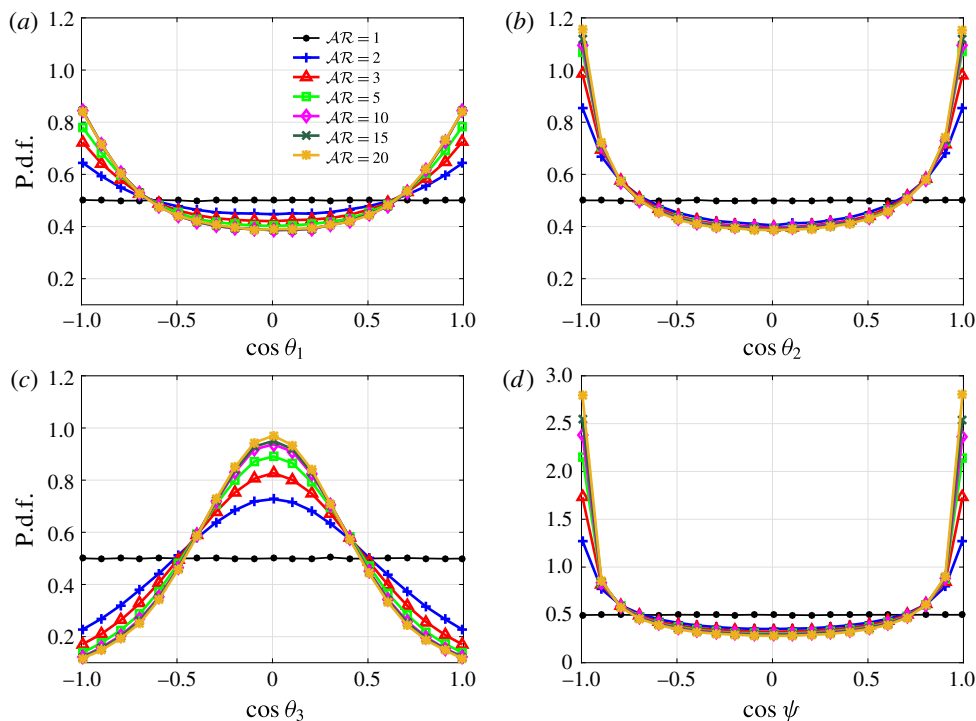


FIGURE 3. (Colour online) Probability density function (p.d.f.) of orientation of particles with different aspect ratios with respect to the three eigenvectors of the deformation tensor (a–c) and the local vorticity vector (d).

changes the average settling speed, v_s^{iso} , and the ratio between maximum and minimum settling speed, v_s^{max}/v_s^{min} , simultaneously. Therefore the saturation in the patchiness and the preferential sampling of regions of downwelling flow can be explained by the change in v_s^{iso} and v_s^{max}/v_s^{min} . A detailed study of each effect is given in the next subsection.

In figure 3, we study the relation between particle orientation and the underlying flow field when varying the particle shape. In figure 3(a–c), we show the orientation of the particle with respect to the three eigendirections of the strain tensor, defined such that $\lambda_1 > \lambda_2 > \lambda_3$ so that the first eigendirection is extensional and the third eigendirection is compressional. The angles between the eigendirections and the spheroid orientation are denoted as θ_1 , θ_2 and θ_3 . In figure 3(d), we show ψ , the angle between the orientation and the local vorticity vector. While spherical particles, $AR = 1$, are isotropic in nature, elongated spheroids tend to align with the local flow strain, more frequently with the second eigendirection, and with the local flow vorticity. Indeed, the p.d.f.s peak when prolate particles are parallel to the eigendirections associated with λ_2 and λ_1 . An increasing probability of parallel alignment with the first two eigendirections of the strain is seen with increased aspect ratio. The spheroid is most likely to be normal to the third eigendirection of the strain, as shown in figure 3(c). The strongest tendency to align with the local vorticity vector is consistent with previous observations for neutrally buoyant spheroids (Chevillard & Meneveau 2013; Ni *et al.* 2015). The alignment with the vorticity vector increases with the aspect ratio AR .

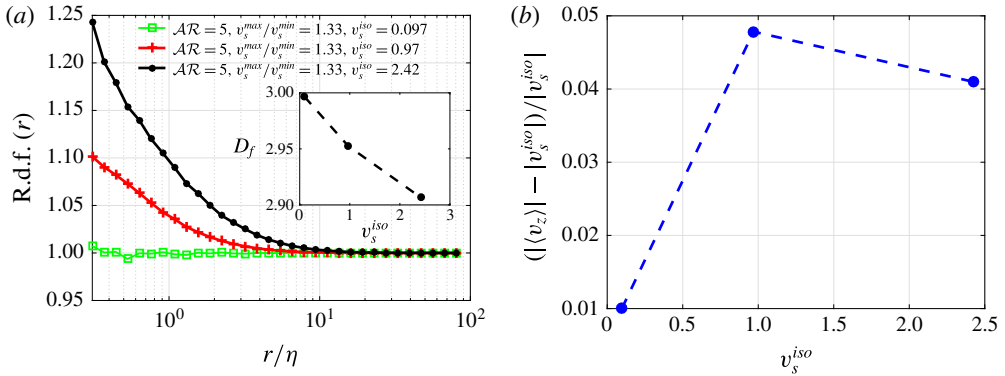


FIGURE 4. (Colour online) (a) Radial distribution function of particle positions and (b) increase in the settling velocity for $\mathcal{AR} = 5$ and the indicated values of v_s^{iso} . Here v_s^{iso} is normalized by the Kolmogorov velocity u_η .

3.1. Numerical experiments

The parameters that define the behaviour of the particles in this regime are the ratio of the amplitude of the sedimenting velocity and the Kolmogorov scale of the turbulence, v_s^{iso}/u_η and the aspect ratio \mathcal{AR} . However, increasing the aspect ratio, while maintaining the mass constant, simultaneously changes the the average settling speed, v_s^{iso} , and the ratio between maximum and minimum settling speed, v_s^{max}/v_s^{min} . In other words, changing the aspect ratio can affect the results by affecting the rotational motion and also by changing sedimentation trajectories. To disentangle these different effects, we perform a series of numerical experiments to investigate separately the effect of the aspect ratio, \mathcal{AR} , the amplitude of the sedimenting velocity v_s^{iso} and the ratio between the maximum (spheroid aligned with the gravity direction) and minimum (normal to gravity) settling speed v_s^{max}/v_s^{min} . In each series of simulations we fix all the parameters except for one to focus on a single parameter effect. While varying only one parameter can result in unrealistic conditions occasionally, it sheds light on the isolated effect of the parameter of interest on particles' collective behaviour. Since phytoplankton exhibits a striking diversity of cell shapes and characteristics, their kinematics can be influenced in important ways, i.e. their characteristics might change their kinematics in a way that these effects get disentangled from each other. For example, an organism that resists falling in a certain direction can increase the drag anisotropy independently of the aspect ratio.

3.1.1. Effect of sedimenting velocity magnitude

First we examine how particle clustering varies with the amplitude of the settling speed. To this end, we keep the aspect ratio $\mathcal{AR} = 5$, corresponding to a ratio between maximum and minimum settling speed, $v_s^{max}/v_s^{min} = 1.33$, and change v_s^{iso} from 0.1 to about 2.5 Kolmogorov velocities (this may correspond to a change in the particle size with respect to the turbulence Kolmogorov scale or a change in particle density). Results in figure 4(a) show that patchiness increases with the average settling speed, as measured by the r.d.f. or by the fractal dimension (inset in figure 4a). The increased clustering, however, does not correspond to an increase of the relative average settling speed when v_s^{iso} is greater than the Kolmogorov velocity.

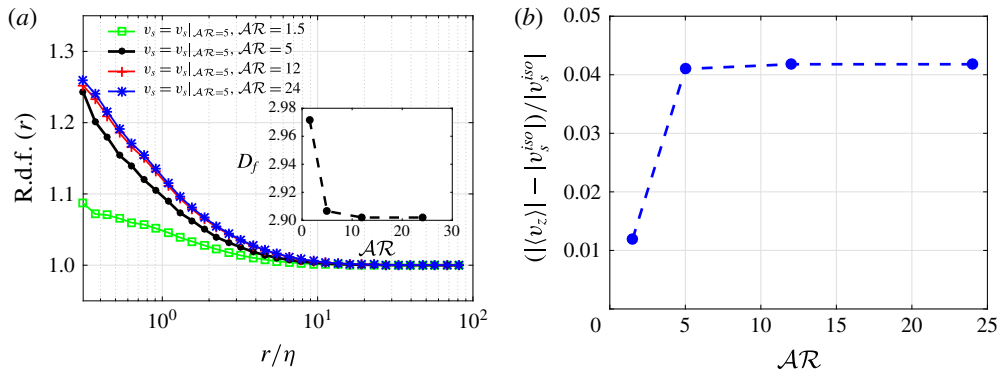


FIGURE 5. (Colour online) (a) Radial distribution function of particle positions and (b) increase in the settling velocity for the different aspect ratios indicated, while keeping the same maximum and minimum settling speed.

3.1.2. Effect of aspect ratio

To elucidate the role of the particle rotation rate on the observed preferential sampling, we vary \mathcal{AR} , while artificially keeping the settling speed fixed, both the components parallel and normal to gravity, at the values corresponding to $\mathcal{AR} = 5$ in table 1. The solution of Jeffery’s equation (2.7) reveals that the time spent aligned with the local shear increases with increasing aspect ratio. The results, displayed in figure 5, show that the r.d.f. and the relative increase of sedimenting velocity saturate for $\mathcal{AR} \geq 5$. Interestingly, rotation rates of oblate and prolate particles are seen to saturate for $\mathcal{AR} > 5$ and for $\mathcal{AR} < 1/5$ in the study of Byron *et al.* (2015). We have also observed, not shown here, that the alignment with the local vorticity increases with the aspect ratio and saturates when $\mathcal{AR} \geq 5$ unlike the cases in figure 3, where it continues to increase; this suggests that the alignment with vorticity is influenced by the difference between settling parallel and normal to gravity, which is fixed here.

3.1.3. Effect of local alignment

As the alignment with the vorticity vector increases with the aspect ratio \mathcal{AR} , see figure 3(d), it is interesting to further explore if preferential alignment contributes to biased sampling and clustering of particles. To show the isolated effect of particle alignment with the local vorticity vector we performed a simulation forcing the elongated spheroid to be always aligned with the local vorticity (figure 6): we observe that clustering decreases in comparison to the case in which the particle was free to rotate. We therefore conclude that clustering cannot be explained by the alignment with the local flow vorticity alone.

3.1.4. Effect of drag anisotropy

One important feature of non-spherical particles in inertialess flows is their drag anisotropy, which can also be exploited by micro-organisms for locomotion. In the case of settling prolate spheroids, this anisotropy is seen in the oblique settling of inclined particles and in the difference between settling speed when oriented parallel or normal to gravity. For the results presented so far we followed the analytical expression for the settling speed derived for prolate spheroids. Shapes in nature are, however, more complicated. Flexibility and non-uniformly distributed mass are likely to cause deviation from the idealized case. To understand more the relevance

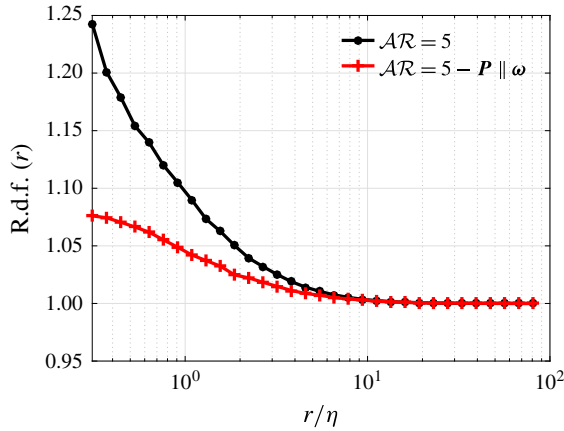


FIGURE 6. (Colour online) Radial distribution function of particle positions for particles with $\mathcal{AR} = 5$ and particles with the same sedimenting velocity but with their orientation forced to be always aligned with the local vorticity vector.

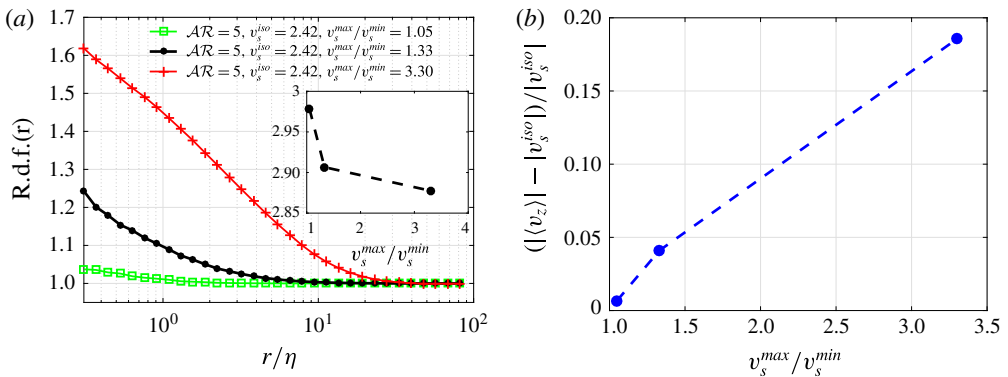


FIGURE 7. (Colour online) (a) Radial distribution function of particle positions and (b) increase in the settling velocity for settling spheroids with aspect ratio $\mathcal{AR} = 5$, fixed average settling speed $v_s^{iso} = 2.42$ and different ratios between settling speed in the direction normal and parallel to gravity, v_s^{max}/v_s^{min} , as indicated in the legend. Here v_s^{iso} is normalized by the Kolmogorov velocity u_η .

of drag anisotropy we perform simulations of spheroids with aspect ratio $\mathcal{AR} = 5$ and fixed average settling speed $v_s^{iso} = 2.42$, while varying the ratio between settling speed in the direction normal and parallel to gravity, v_s^{max}/v_s^{min} . As seen in figure 7(a) clustering increases significantly with drag anisotropy, or v_s^{max}/v_s^{min} . More interestingly, the relative settling speed increases by up to about 20% when $v_s^{max}/v_s^{min} = 3.3$. The value 3.3 is chosen to artificially emphasize the drag anisotropy effect; note that the ratio between maximum and minimum settling speed of spheroidal particles increases with the aspect ratio and saturates at about 1.75 (figure 8).

3.2. Mechanism for increased settling speed

To understand why ellipsoidal particles preferentially locate in regions of downwelling flow and thus have an enhanced settling speed, we consider a vertical linear shear,

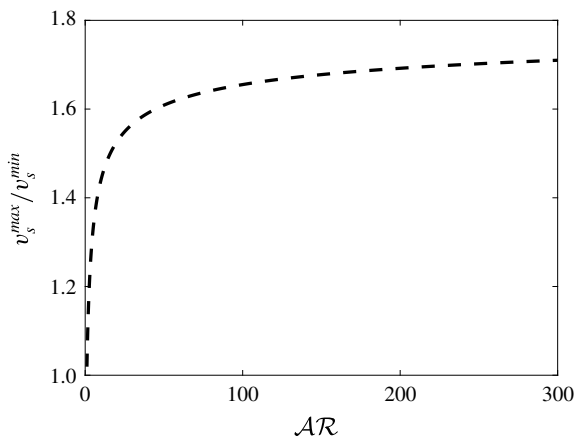


FIGURE 8. Plot of v_s^{max}/v_s^{min} versus \mathcal{AR} for prolate particles, see e.g. analytical expressions reported in Dahlkild (2011).

$\mathbf{u} = -\gamma x \hat{\mathbf{e}}_g$ with motion constrained to the x - z plane. We define θ to be the angle the particle symmetry axis makes with the vertical, so that in x - z co-ordinates the orientation vector is given by $\mathbf{p} = (\sin \theta, \cos \theta)^T$.

From Jeffery’s equation (2.7) the time evolution of particle orientation is given by

$$\dot{\theta} = \frac{\gamma}{2} (-1 + \alpha \cos 2\theta). \tag{3.3}$$

Note that the particle rotates most slowly when $\theta = 0$ or π , and thus spends more time in these states, i.e. aligned with the local shear. From (2.5), the vertical velocity of a particle is given by

$$v_z = \gamma x - v_s^{min} - (v_s^{max} - v_s^{min}) \cos^2 \theta. \tag{3.4}$$

The time-averaged vertical velocity over a Jeffery orbit (of duration $T = 4\pi/\gamma\sqrt{1-\alpha^2}$) is given by

$$\begin{aligned} \bar{v}_z &= \frac{1}{T} \int_0^T (\gamma x - v_s^{min} - (v_s^{max} - v_s^{min}) \cos^2 \theta) dt \\ &= \gamma \bar{x} - v_s^{min} - \frac{(v_s^{max} - v_s^{min}) \sqrt{1-\alpha^2}}{2\pi} \int_0^{2\pi} \frac{\cos^2 \theta}{-1 + \alpha \cos 2\theta} d\theta, \end{aligned} \tag{3.5}$$

where \bar{x} is the time-averaged horizontal position. The effect of the shear strength, γ , only appears through the term $\gamma \bar{x}$, and so the effect of the shear on the total vertical velocity of particles can be determined if we know the time-averaged horizontal position. In particular, the only way cells are predicted to exhibit enhanced settling is if they spend more time in downwelling regions.

To demonstrate how the time-averaged horizontal position is biased towards downwelling regions, yielding enhanced settling, we numerically compute particle trajectories for a complete Jeffery orbit for an example set of parameters taken from table 1: $\gamma = 1$, $\mathcal{AR} = 20$ ($\alpha = 0.995$), $v_s^{min} = 1.29$ and $v_s^{max} = 1.97$ (see figure 9).

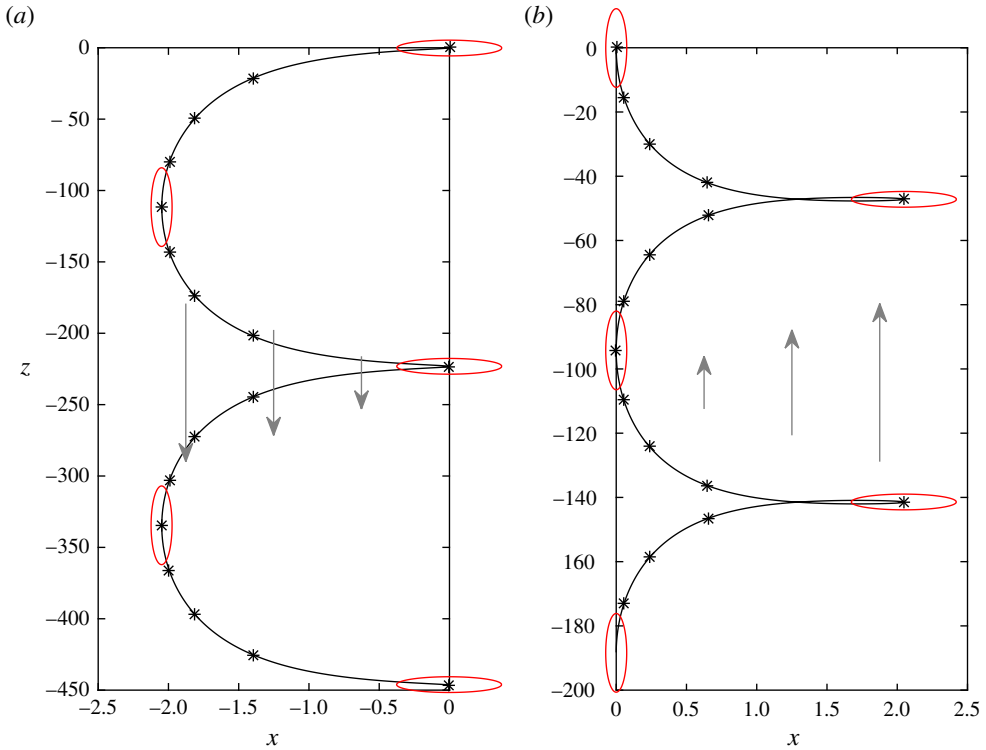


FIGURE 9. (Colour online) Trajectory of single particle in vertical laminar shear over a Jeffery orbit. Particle initially at the origin with orientation (a) $\theta = \pi/2$ and (b) $\theta = 0$. Stars indicate position at equally spaced time intervals, red ellipses indicate particle orientation. Grey arrows indicate flow velocity $\mathbf{u} = -\gamma x \hat{\mathbf{e}}_g$.

Particles are initially located at the origin, and the initial orientation is taken as $\theta = 0$ or $\theta = \pi/2$. Particles initially horizontal ($\theta = \pi/2$, figure 9a) have a negative horizontal (parallel to the direction of the flow) component due to shear-induced lift, causing them to translate into downwelling flow. As the particle rotates, it reaches a minimum horizontal position at the point when $\theta = 0$ and then reverses its horizontal component of motion back towards $x = 0$ which is attained when $\theta = 3\pi/2$. The particle has a slowest rotation rate when $\theta = 0$ or π , corresponding to the minimum horizontal position, and thus the time-averaged horizontal position is less than the midpoint of the horizontal limits of the trajectory. This bias represents a tendency to cluster in downwelling flow. Particles initially vertical ($\theta = 0$, figure 9b) sediment with a positive horizontal component into upwelling flow. As the particle rotates, it reaches a maximum horizontal position at the point when $\theta = 3\pi/2$ and then reverses its horizontal component of motion back towards $x = 0$, which is attained when $\theta = \pi$. Again, the particle has a slowest rotation rate at the minimum horizontal position (horizontal distance from origin), and thus the time-averaged horizontal position is less than the midpoint of the horizontal limits of the trajectory (horizontal distance from origin is larger). This simple example shows how shear, rotation, lift, and drag-anisotropy couple to bias particle trajectories towards downward flow. These simpler model shows that drag anisotropy can increase the bias towards regions of

negative fluid velocity, and therefore explains the sensitivity of the results to the ratio between maximum and minimum sedimentation velocity v_s^{max}/v_s^{min} (see § 3.1.4).

Note finally that this mechanism for preferential sampling of downwelling flows is similar to the one reported by Koch & Shaqfeh (1989) when studying the instability of a dispersion of sedimenting spheroids. In their study, however, the vertical shearing motion was induced by the velocity disturbance of a neighbouring spheroid while we assume here a constant background shear.

4. Final remarks

We report results from simulations of elongated, rigid particles (prolate spheroids) with different aspect ratios sinking in homogenous, isotropic turbulence. The parameters used in this study represent marine or freshwater diatoms that are characterized by very small relaxation times compared to that of the fluid but with settling velocities on the order of Kolmogorov velocities characteristic of the mixed layer in the ocean. Given the small size of diatoms relative to the Kolmogorov length-scale and their short relaxation time, cells are assumed to behave like passive tracers with a correction given by their Stokes settling velocity. We show that turbulence does increase the settling velocities of inertia-less elongated particles, compared to their Stokes settling velocities, and that the effect increases as the aspect ratio of the particle increases, but saturates at $\mathcal{AR} \geq 10$. The magnitude of this effect, however, is small ($\sim 5\%$, figure 2c). It should be noted that despite the enhanced mean settling velocity for diatoms reported in this study, there could be dispersion of particles in turbulent flow that increases the residence time of some individuals.

Further, we study homogenous isotropic turbulence at the dissipation scale, and thus neglect large-scale turbulence that might play a role in suspending diatoms. Indeed, the question ‘How local enhancement is related to residence time in the mixed layer of the ocean?’ is still unanswered and might be very well related to the large scale turbulence that is not captured in the current model. In our model, turbulence dissipation rate, ϵ , was set to $10^{-6} \text{ m}^2 \text{ s}^{-3}$. This choice is within the range observed in the ocean’s surface boundary layer in a coastal environment (Gerbi *et al.* 2009). For this turbulence level, settling is slightly enhanced. Ruiz *et al.* (2004) used a Couette device to generate turbulence and showed that sinking speeds of different species of phytoplankton increased significantly (by an order of magnitude for some species) as ϵ increased from $\epsilon < 10^{-6} \text{ m}^2 \text{ s}^{-3}$ to $\epsilon > 10^{-4} \text{ m}^2 \text{ s}^{-3}$. They also showed that downward velocities increased as the ratio between the size of the cell (described as equivalent spherical diameter in their study) and the Kolmogorov length-scale increased (Ruiz *et al.* 2004).

Here we show that non-random distributions can arise within the parameter space relevant to diatoms, with weak clustering occurring only for non-spherical cells. Preferential sampling of downwelling flow is due to the interactions between shear, particle rotation, drag, and lift. Elongated spheroids tend to align with the local flow strain (more frequently with the second eigen-direction) and with the local flow vorticity, in agreement with previous studies on neutrally buoyant spheroids in homogenous isotropic turbulence (e.g. Ni *et al.* (2015), Voth & Soldati (2017) and references therein). By considering the simple case of one particle sedimenting in linear shear flow we demonstrate that the time-averaged horizontal position of a particle in the flow (over a complete Jeffery orbit) is biased towards downwelling regions. Spheroids with higher average Stokes settling speeds (v_s^{iso}) show greater tendency to cluster (see figure 4a). However, when v_s^{iso} is greater than the Kolmogorov

velocity, the increase in clustering does not correspond to an increase in relative average settling speed. We also show that clustering increases significantly with drag anisotropy (i.e. the ratio v_s^{max}/v_s^{min}) in a way that does not appear to saturate. Drag anisotropy increases with increasing \mathcal{AR} and forces particles to sample regions of downwelling flow to a further extent, even when the isolated effect of aspect ratio on the rotational motion is saturated.

Mechanisms that affect sinking and dispersion of phytoplankton hold significant implications to carbon and energy fluxes in aquatic systems. Underlying distributions of phytoplankton at the micro-scale are not well understood as we still lack the tools to measure them in the field. Few available observations suggest that at scales of centimeters, the seascape is more heterogeneous than previously thought (Malkiel, Alquaddoomi & Katz 1999; Seuront, Schmitt & Lagadeuc 2001; Mitchell *et al.* 2008) but mechanisms remain poorly understood. This study provides insights into one mechanism by which weak clustering of chains and elongated cells of diatoms can occur at the millimetre to centimetre scale. A typical fractal dimension of 2.8–2.9 shows a weak clustering, and it might be that other mechanisms exist behind the clustering that our model cannot capture.

Cell shape is an important morphological trait affecting many aspects in the ecology of phytoplankton (Smayda 1970; Lewis 1976; Sournia 1982; Reynolds 1989; Reynolds & Irish 1997; Karp-Boss & Boss 2016) and results from our numerical model further highlight the complex interactions of cell shape with ambient flows. Interestingly, the observed increase in settling speeds does not increase indefinitely, and saturates for $\mathcal{AR} > 10$. Increasing the aspect ratio, while keeping the particle volume and density ratio constant, varies other characteristics of the particle simultaneously. For example, the mean settling speed in quiescent flow decreases as the ratio between maximum (when particle is oriented parallel to the gravity direction) and minimum (when particle is oriented normal to the gravity direction) settling speed increases. We have therefore performed a series of numerical experiments to isolate the effect of the aspect ratio \mathcal{AR} , the magnitude of settling velocity v_s^{iso} and the ratio between the maximum and minimum settling speed v_s^{max}/v_s^{min} in quiescent flow. When v_s^{iso} and v_s^{max}/v_s^{min} are held constant, the increase in clustering and settling speed begins to saturate at $\mathcal{AR} = 5$. This indicates that the relative enhancement that we observe for ellipsoids with aspect ratios larger than 5 is due to an increase in the ratio between the maximum and minimum settling speed (v_s^{max}/v_s^{min}) that is associated with a change in particle shape (\mathcal{AR} at constant volume). Interestingly, an analysis of typical aspect ratios among phytoplankton shows a peak in distribution at $\mathcal{AR} \sim 5$ (Clavano, Boss & Karp-Boss 2007; Karp-Boss & Boss 2016), but this may be a coincidence because in nature multiple processes (grazing, diffusion, mechanical breakage by shear) act simultaneously as selective pressures on shape and size in phytoplankton (Karp-Boss & Boss 2016).

The model presented here is an idealized case of turbulence and phytoplankton in the ocean. Direct numerical simulations are computationally expensive and cannot be used to capture the full range of scales characteristic of oceanic turbulence, and are limited to low Reynolds numbers. We consider homogeneous isotropic turbulence, but in the ocean most turbulent mixing occurs near boundaries and is subjected to stratification and vertical shear. It was found, however, that in stratified regions of the ocean, isotropic motions do exist over some range of scale bounded at the lower end by the Kolmogorov length scale, providing that the non-dimensional isotropy parameter $I = \epsilon/\nu N^2$ exceeds ~ 200 , where ϵ is the local mean kinetic energy dissipation, ν the kinematic viscosity and N the local mean value of the buoyancy frequency (Thorpe 2007).

Modelling phytoplankton as rigid prolate spheroids with an even distribution of mass is another simplification of the model. Diatoms exhibit complex morphologies (see figure 1) and often bear spines and other cell projections that can alter dynamics in the flow. Another attribute of chain-forming diatoms that is dynamically important is flexural stiffness, as it spans four orders of magnitude between different species (Young 2011). Variations in rotation rates between rigid and flexible particles were observed in a laboratory setting (Karp-Boss & Jumars 1998), and it is likely that rigid and flexible chains will also exhibit different dynamics in turbulence, a subject that requires more investigations in the future.

Acknowledgements

M.N.A., G.S. and L.B. acknowledge support by the European Research Council grant no. ERC-2013-CoG-616186, TRITOS and the Swedish Research Council grant Outstanding Young Researcher to L.B. Computer time is provided by SNIC (Swedish National Infrastructure for Computing). We also acknowledge the support from the COST Action MP1305: Flowing matter, with particular mention to the discussions held during the workshop ‘Microorganisms in Turbulent Flows’, Lorentz Centre, Leiden, the Netherlands. This work is also supported by the National Science Foundation (NSF) grant no. 1334365 to L.K.-B. and grants nos 1334788 and 1604026 to E.A.V.

Appendix. Parameter space for phytoplankton

Dissipation rates of turbulent kinetic energy ϵ in the ocean vary greatly in space and time. In the open ocean, typical values range from 10^{-10} to 10^{-7} $\text{m}^2 \text{s}^{-3}$, while coastal regions, especially those influenced by tidal fronts, experience higher dissipation rates, on the order of 10^{-7} to 10^{-4} $\text{m}^2 \text{s}^{-3}$ (Smyth & Moum 2000; Barton *et al.* 2014). Within the water column, turbulence kinetic energy dissipation rates are higher at the surface and decrease with depth (Smyth & Moum 2000). Given the kinematic viscosity of seawater $\nu \sim 10^{-6}$ $\text{m}^2 \text{s}^{-1}$, the characteristic Kolmogorov length scale η in the ocean ranges from ~ 300 μm to a few millimetres. Generally speaking, diatoms are smaller than characteristic Kolmogorov length scales in the ocean, and range in size from a few micrometres for small solitary cells to hundreds of micrometres in length for chain-forming species (Karp-Boss & Jumars 1998). This size ratio may become order 1 for very long chains in strong turbulence, but this would represent an extreme case. Sinking velocities of diatoms have been measured in quiescent water by measuring the temporal change in concentration of diatoms at the top and bottom of a water column with a known height and calculating average (community) settling velocities. Using this approach, settling velocities (v_s^{iso}) were found to range between 2 $\mu\text{m s}^{-1}$ and ~ 1 mm s^{-1} (reviewed in Smayda 1970).

Characteristic velocities at dissipation scale in the ocean ($u_\eta = (\nu\epsilon)^{1/4}$) are on the order of 0.01–0.1 mm s^{-1} , resulting in a velocity ratio $v_s^{iso}/u_\eta \approx 1$ –4 (assuming maximum v_s^{iso} of 1 mm s^{-1}). Densities of marine diatoms ρ_p have not been measured directly but estimated from the Stokes equation for settling spheres, based on measured sinking velocities. Densities were found to be in the range 1.03–1.15 g cm^{-3} for actively growing cells with higher values for cells in senescence (1.059–1.33 g cm^{-3} ; Eppley *et al.* 1967). Average density of surface seawater ρ_f is 1.025 g cm^{-3} and thus the density ratio relevant to the parameter space of phytoplankton is in the range 1–1.3. Table 2 summarizes the parameter values relevant to marine diatoms.

Parameter	Values
Kinetic energy dissipation rate (ϵ)	10^{-10} – 10^{-4} m ² s ⁻³
Taylor Reynolds number (Re_λ)	50–200
Sinking velocity of diatoms (v_s^{iso})	2 μ m s ⁻¹ –1 mm s ⁻¹
Velocity ratio (v_s^{iso}/u_η)	0.02–11
Size ratio (L/η)	0.003–2
Density ratio (ρ_p/ρ_f)	1–1.3
Relaxation time of a cell (τ_p)	$\sim 10^{-4}$ s
Relaxation time of fluid (τ_f)	~ 1 s
Stokes number (τ_p/τ_f)	$\sim 10^{-4}$

TABLE 2. A summary of the parameter values relevant to marine diatoms. The value of ϵ is considered 10^{-6} m² s⁻³ for calculating τ_f and Re_λ .

REFERENCES

- ANDERSSON, H. I., ZHAO, L. & BARRI, M. 2012 Torque-coupling and particle–turbulence interactions. *J. Fluid Mech.* **696**, 319–329.
- BARTON, A. D., WARD, B. A., WILLIAMS, R. G. & FOLLOWS, M. J. 2014 The impact of fine-scale turbulence on phytoplankton community structure. *Limnol. Oceanogr.* **4** (1), 34–49.
- BEC, J., HOMANN, H. & RAY, S. S. 2014 Gravity-driven enhancement of heavy particle clustering in turbulent flow. *Phys. Rev. Lett.* **112** (18), 184501.
- BUTLER, J. E. & SHAQFEH, E. S. 2002 Dynamic simulations of the inhomogeneous sedimentation of rigid fibres. *J. Fluid Mech.* **468**, 205–237.
- BYRON, M., EINARSSON, J., GUSTAVSSON, K., VOTH, G., MEHLIG, B. & VARIANO, E. 2015 Shape-dependence of particle rotation in isotropic turbulence. *Phys. Fluids* **27** (3), 035101.
- CHEVILLARD, L. & MENEVEAU, C. 2013 Orientation dynamics of small, triaxial–ellipsoidal particles in isotropic turbulence. *J. Fluid Mech.* **737**, 571–596.
- CLAVANO, W. R., BOSS, E. & KARP-BOSS, L. 2007 Inherent optical properties of non-spherical marine-like particles from theory to observation. *Oceanogr. Mar. Biol. Annu. Rev.* **45**, 1–38.
- DAHLKILD, A. A. 2011 Finite wavelength selection for the linear instability of a suspension of settling spheroids. *J. Fluid Mech.* **689**, 183–202.
- DURHAM, W. M., CLIMENT, E., BARRY, M., DE LILLO, F., BOFFETTA, G., CENCINI, M. & STOCKER, R. 2013 Turbulence drives microscale patches of motile phytoplankton. *Nature Commun.* **4**, 2148.
- EPPLEY, R. W., HOLMES, R. W. & STRICKLAND, J. D. H. 1967 Sinking rates of marine phytoplankton measured with a fluorometer. *J. Exp. Marine Biol. Ecol.* **1** (2), 191–208.
- GERBI, G. P., TROWBRIDGE, J. H., TERRAY, E. A., PLUEDDEMANN, A. J. & KUKULKA, T. 2009 Observations of turbulence in the ocean surface boundary layer: energetics and transport. *J. Phys. Oceanogr.* **39** (5), 1077–1096.
- GUAZZELLI, E. & HINCH, J. 2011 Fluctuations and instability in sedimentation. *Annu. Rev. Fluid Mech.* **43**, 97–116.
- GUAZZELLI, E. & MORRIS, J. F. 2011 *A Physical Introduction to Suspension Dynamics*, vol. 45. Cambridge University Press.
- GUSTAVSSON, K. & TORNBORG, A. K. 2009 Gravity induced sedimentation of slender fibers. *Phys. Fluids* **21** (12), 123301.
- GUSTAVSSON, K., VAJEDI, S. & MEHLIG, B. 2014 Clustering of particles falling in a turbulent flow. *Phys. Rev. Lett.* **112** (21), 214501.
- HERZHAFT, B. & GUAZZELLI, E. 1999 Experimental study of the sedimentation of dilute and semi-dilute suspensions of fibres. *J. Fluid Mech.* **384**, 133–158.
- HERZHAFT, B., GUAZZELLI, E., MACKAPLOW, M. B. & SHAQFEH, E. S. 1996 Experimental investigation of the sedimentation of a dilute fiber suspension. *Phys. Rev. Lett.* **77** (2), 290.

- JEFFERY, G. B. 1922 The motion of ellipsoidal particles immersed in a viscous fluid. In *Proceedings of the Royal Society of London A: Mathematical, Physical and Engineering Sciences*, vol. 102, pp. 161–179. The Royal Society.
- KARP-BOSS, L. & BOSS, E. 2016 The elongated, the squat and the spherical: selective pressures for phytoplankton shape. In *Aquatic Microbial Ecology and Biogeochemistry: A Dual Perspective*, pp. 25–34. Springer.
- KARP-BOSS, L. & JUMARS, P. A. 1998 Motion of diatom chains in steady shear flow. *Limnol. Oceanogr.* **43**, 1767–1773.
- KOCH, D. L. & SHAQFEH, E. S. 1989 The instability of a dispersion of sedimenting spheroids. *J. Fluid Mech.* **209**, 521–542.
- LEWIS, W. M. 1976 Surface/volume ratio: implications for phytoplankton morphology. *Science* **192** (4242), 885–887.
- MACKAPLOW, M. B. & SHAQFEH, E. S. 1998 A numerical study of the sedimentation of fibre suspensions. *J. Fluid Mech.* **376**, 149–182.
- MALKIEL, E., ALQUADDOOMI, O. & KATZ, J. 1999 Measurements of plankton distribution in the ocean using submersible holography. *Meas. Sci. Technol.* **10** (12), 1142.
- MALLIER, R. & MAXEY, M. 1991 The settling of nonspherical particles in a cellular flow field. *Phys. Fluids A* **3** (6), 1481–1494.
- MARCHIOLI, C., FANTONI, M. & SOLDATI, A. 2010 Orientation, distribution, and deposition of elongated, inertial fibers in turbulent channel flow. *Phys. Fluids* **22** (3), 033301.
- MARCHIOLI, C., ZHAO, L. & ANDERSSON, H. I. 2016 On the relative rotational motion between rigid fibers and fluid in turbulent channel flow. *Phys. Fluids* **28** (1), 013301.
- MARGALEF, R. 1978 Life-forms of phytoplankton as survival alternatives in an unstable environment. *Oceanol. Acta* **1** (4), 493–509.
- MITCHELL, J. G., YAMAZAKI, H., SEURONT, L., WOLK, F. & LI, H. 2008 Phytoplankton patch patterns: seascape anatomy in a turbulent ocean. *J. Mar. Syst.* **69** (3), 247–253.
- NGUYEN, H., KARP-BOSS, L., JUMARS, P. A. & FAUCI, L. 2011 Hydrodynamic effects of spines: a different spin. *Limnol. Oceanogr.* **1** (1), 110–119.
- NI, R., KRAMEL, S., OUELLETTE, N. T. & VOTH, G. A. 2015 Measurements of the coupling between the tumbling of rods and the velocity gradient tensor in turbulence. *J. Fluid Mech.* **766**, 202–225.
- OLSON, J. A. & KEREKES, R. J. 1998 The motion of fibres in turbulent flow. *J. Fluid Mech.* **377**, 47–64.
- PARSA, S., CALZAVARINI, E., TOSCHI, F. & VOTH, G. A. 2012 Rotation rate of rods in turbulent fluid flow. *Phys. Rev. Lett.* **109** (13), 134501.
- PARSA, S. & VOTH, G. A. 2014 Inertial range scaling in rotations of long rods in turbulence. *Phys. Rev. Lett.* **112** (2), 024501.
- PUMIR, A. & WILKINSON, M. 2011 Orientation statistics of small particles in turbulence. *New J. Phys.* **13** (9), 093030.
- REYNOLDS, C. S. 1989 Physical determinants of phytoplankton succession. In *Plankton Ecology*, pp. 9–56. Springer.
- REYNOLDS, C. S. & IRISH, A. E. 1997 Modelling phytoplankton dynamics in lakes and reservoirs: the problem of *in-situ* growth rates. *Hydrobiologia* **349** (1–3), 5–17.
- ROGALLO, R. S. 1981 Numerical experiments in homogeneous turbulence. *NASA STI/Recon Tech. Rep.* N 81, 31508.
- RUIZ, J., MACÍAS, D. & PETERS, F. 2004 Turbulence increases the average settling velocity of phytoplankton cells. *Proc. Natl Acad. Sci. USA* **101** (51), 17720–17724.
- SARDINA, G., PICANO, F., BRANDT, L. & CABALLERO, R. 2015 Continuous growth of droplet size variance due to condensation in turbulent clouds. *Phys. Rev. Lett.* **115** (18), 184501.
- SEURONT, L., SCHMITT, F. & LAGADEUC, Y. 2001 Turbulence intermittency, small-scale phytoplankton patchiness and encounter rates in plankton: where do we go from here? *Deep-Sea Res. (I)* **48** (5), 1199–1215.
- SHAPIRO, M. & GOLDENBERG, M. 1993 Deposition of glass fiber particles from turbulent air flow in a pipe. *J. Aerosol Sci.* **24** (1), 65–87.

- SHIN, H. & MAXEY, M. R. 1997 Chaotic motion of nonspherical particles settling in a cellular flow field. *Phys. Rev. E* **56** (5), 5431.
- SHIN, M. & KOCH, D. L. 2005 Rotational and translational dispersion of fibres in isotropic turbulent flows. *J. Fluid Mech.* **540**, 143–173.
- SIEWERT, C., KUNNEN, R. P. J., MEINKE, M. & SCHRÖDER, W. 2014 Orientation statistics and settling velocity of ellipsoids in decaying turbulence. *Atmospheric Res.* **142**, 45–56.
- SMAYDA, T. J. 1970 The suspension and sinking of phytoplankton in the sea. *Ann. Rev. Oceanogr. Mar. Biol.* **8**, 353–414.
- SMYTH, W. D. & MOUM, J. N. 2000 Ocean turbulence. *Tech. Rep.* College of Oceanic and Atmospheric Sciences, Oregon State University.
- SOURNIA, A. 1982 Form and function in marine phytoplankton. *Biol. Rev.* **57** (3), 347–394.
- THORPE, S. A. 2007 *An Introduction to Ocean Turbulence*. Cambridge University Press.
- TOSCHI, F. & BODENSCHATZ, E. 2009 Lagrangian properties of particles in turbulence. *Annu. Rev. Fluid Mech.* **41**, 375–404.
- VINCENT, A. & MENEGUZZI, M. 1994 The dynamics of vorticity tubes in homogeneous turbulence. *J. Fluid Mech.* **258**, 245–254.
- VOTH, G. A. & SOLDATI, A. 2017 Anisotropic particles in turbulence. *Annu. Rev. Fluid Mech.* **49**, 249–276.
- WANG, L. P. & MAXEY, M. R. 1993 Settling velocity and concentration distribution of heavy particles in homogeneous isotropic turbulence. *J. Fluid Mech.* **256**, 27–68.
- WANG, L. P. & STOCK, D. E. 1993 Dispersion of heavy particles by turbulent motion. *J. Atmos. Sci.* **50** (13), 1897–1913.
- YOUNG, A. M. 2011 Quantifying diatom aspirations: mechanical properties of chain-forming species. PhD thesis, The University of Maine.
- ZHAN, C., SARDINA, G., LUSHI, E. & BRANDT, L. 2014 Accumulation of motile elongated microorganisms in turbulence. *J. Fluid Mech.* **739**, 22–36.
- ZHANG, H., AHMADI, G., FAN, F. G. & MCLAUGHLIN, J. B. 2001 Ellipsoidal particles transport and deposition in turbulent channel flows. *Intl J. Multiphase Flow* **27** (6), 971–1009.
- ZHAO, L., CHALLABOTLA, N. R., ANDERSSON, H. I. & VARIANO, E. A. 2015 Rotation of nonspherical particles in turbulent channel flow. *Phys. Rev. Lett.* **115** (24), 244501.